IEEE Access
Multidisciplinary | Rapid Review | Open Access Journal

Received July 8, 2019, accepted July 15, 2019, date of publication July 18, 2019, date of current version August 16, 2019.

Digital Object Identifier 10.1109/ACCESS.2019.2929516

A Flexible Wireless Power Transfer System With Switch Controlled Capacitor

JIN ZHAO[1], (Student Member, IEEE), JIANZHONG ZHANG[1], (Senior Member, IEEE), AND YAODONG ZHU[2]

[1]School of Electrical Engineering, Southeast University, Nanjing 210096, China
[2]School of Mechanical and Electrical Engineering, Jiaxing University, Jiaxing 314001, China

Corresponding author: Jianzhong Zhang (jiz@seu.edu.cn)

This work was supported in part by the National Natural Science Foundation of China (NSFC) under Grant 51577025, and in part by the Zhejiang Key Research and Development Project under Grant 2017C01043.

ABSTRACT Wireless power transfer (WPT) with a switch-controlled capacitor (SCC) is proposed in this paper for compensating load impedance which is related to the coupling coefficient of coils and the load variations. In general, the power supply in the WPT system is desired to output constant voltage under varied load impedance. In the proposed WPT system, the resonant capacitor in the primary side is replaced by an SCC and only diode full-bridge rectifier in the secondary side is used. The SCC realizes adjustable capacitor which makes it flexible to control the capacitance. At the same time, the modulation of the SCC aims to guarantee an inductive input impedance of the WPT system, achieving soft switching and reducing the high switching losses of the high-frequency inverter. In order to verify the feasibility of the proposed method, mathematical analysis, and experimental validations have been thoroughly performed. The experiment results show that the WPT system maintains a stable output voltage by through the regulation of the SCC according to the load variations.

INDEX TERMS Resonant inverter, switch-controlled capacitor, WPT, zero voltage switching.

I. INTRODUCTION

Wireless power transfer (WPT) technology with the magnetic field utilize coupling coils to transfer energy through a relatively large air gap and can get rid of the restraint of the cable [1], [2]. With the merit of convenience and safety, WPT has employed in many charging applications, for the low-power application of several watts such as smartphones [3], [4] or biomedical implants [5], for the medium power application of several kilowatts such as charging electric vehicle [6], [7], and even for the mega-watts application such as the trains [8].

So far, extensive work both in theoretical analysis as well as practical aspects of design for WPT systems has been done by researcher around the world. In most of the literatures, either the maximum efficiency principle or maximum power transfer principle have been discussed, but the design of high-frequency power converters for WPT system has rarely been discussed [9].

The associate editor coordinating the review of this manuscript and approving it for publication was Tawfik Al-Hadhrami.

Generally, the WPT systems are desired to provide a constant output voltage against to the variations of load impedance. The load impedance is related to the coupling coefficient and load capacity and usually is a time varying parameter in practical system. Taking the typical battery load as an example, the equivalent resistance of battery varies in a wide range during the whole charging or discharging process. For realizing the desired stable output voltage against a variable load impedance for WPT systems, [5], [10], [11] achieve stable voltage gain against varied load and coupling factors by tracking split frequencies. However, the stability problem caused by the frequency bifurcation phenomenon does not been fully considered. [12], [13] use a dc/dc converter in primary side or secondary side, which is also an effective way to regulate the output voltage. However, the converters cost a lot and introduce additional losses. [14], [15] adopt the dynamic impedance matching circuits to maximize the power transfer. This method can also be applied to regulate the output voltage.

To improve the performance of the WPT system, resonance capacitor is needed to compensate the inductive reactance of the coil. There are four basic resonant topologies

according to the connection circuit of the resonance capacitors, including series-series, series-parallel, parallel-parallel and parallel-series topologies [16]. Moreover, the resonant topologies with more than four elements are also developed for the WPT systems. However, more resonant elements increase the cost and complicate the design. In addition, the inductor and capacitor normally have large manufacturing tolerance, and the inductance and capacitance may be deviated due to aging [17]. This will further reduce the performance of the WPT system.

In this paper, a switch-controlled capacitor (SCC), connected in the primary side, is introduced to compensate the inductive reactance of the coil. By controlling the equivalent capacitance of the SCC, the inverter could keep in resonance operation and the performance of the WPT system can be enhanced with the ZVS operation achieved by modulating the SCC to an inductive load for the inverter. Only the diode full-bridge rectifier is use in the secondary side where the capacitor is removed. It is beneficial for integration and can be applied to more application backgrounds.

This paper is organized as follows. In section II, the circuit configuration is proposed. In section III, the corresponding control strategy for the proposed system is presented. The control method is validated by experiments in section IV. Finally, the conclusions are drawn in section V.

II. CIRCUIT CONFIGURATIONS

A. SCC

The concept of SCC was proposed in [18] to regulate the resonant converters with fixed operating frequency. The SCC is used to regulate the equivalent capacitance, and thus to control the resonant frequency of the inverter. The controllable resonant frequency in turn controls the output of converters. In the proposed WPT system of this paper, the SCC in the primary side is regulated not only for compensating the load impedance, but also for producing soft-switching condition.

Figure 1 shows the circuit structure and the operation waveforms of the SCC. As shown in Figure 1(a), the SCC consists of two source-to-source connected MOSFET switches, S_a and S_b, and a parallel linear capacitor C_a.

A sinusoidal current i_{ab} is applied to the SCC from terminal a to terminal b, as shown in Figure 1(b). It has

$$i_{ab} = I_{ab}\sin(\omega_0 t) \tag{1}$$

where I_{ab} is the amplitude of the input current and ω_0 is the angular frequency of the input current. Gate signals for driving the switches S_a and S_b are synchronized with current i_{ab}. They have phase shift α from i_{ab} and are complementary each other, as shown in Figure 1(b). In the interval of $[\alpha, \alpha+\varphi]$, the voltage across the C_a is

$$u_{ab} = \frac{1}{C_a}\int_{\alpha}^{\omega_0 t} I_{ab}\sin(\omega_0 t)dt = \frac{I_{ab}}{\omega C_a}[\cos\alpha - \cos(\omega_0 t)] \tag{2}$$

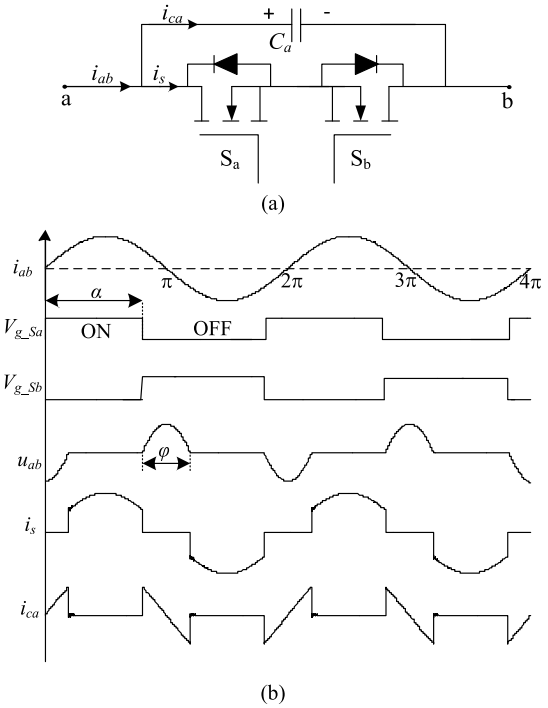

FIGURE 1. SCC, (a) Structure; (b) operation waveforms.

When $\omega t = \alpha + \varphi$, $u_{ab} = 0$, substituting it into (2). It has

$$\alpha = \pi - \frac{\varphi}{2} \tag{3}$$

The voltage amplitude of the fundamental component can be calculated by Fourier series from (2). It has

$$\begin{aligned} U_{ab(1)} &= \frac{2}{\pi}\int_{\alpha}^{\alpha+\varphi} u_{ab}\cos(\omega_0 t)d(\omega t) \\ &= \frac{I_{ab}}{\omega_0}\cdot\left[-(\pi - \alpha + \frac{1}{2}\sin 2\alpha)\frac{2}{\pi C_a}\right] \end{aligned} \tag{4}$$

where $U_{ab(1)}$ is the voltage amplitude of the fundamental component. From (4), the equivalent capacitance of the SCC can be expressed as

$$C_{sc} = \frac{\pi C_a}{2\pi - 2\alpha + \sin 2\alpha} \tag{5}$$

where C_{sc} is the equivalent capacitance of the SCC. Figure 2 shows the capacitance ratio between the equivalent capacitance C_{sc} and parallel capacitor C_a with respect to the changes of α by use of (5). It is clearly shown in Figure 2 that the equivalent capacitance C_{sc} can be regulated effectively by changing α. In the case of $\alpha = \pi/2$, where the capacitance ratio C_{sc}/C_a equals 1, the capacitor C_a is always connected with the circuit and the current flows continuously from terminal a to terminal b. The switches S_a and S_b are effectively OFF all the time, and there is no current flowing through them. In the case of $\alpha = \pi$, there is no current flowing from terminal a to terminal b. The capacitor C_a is always by-passed by switches which are effectively ON all the time. In this case, the SCC performs as a capacitor with infinite capacitance.

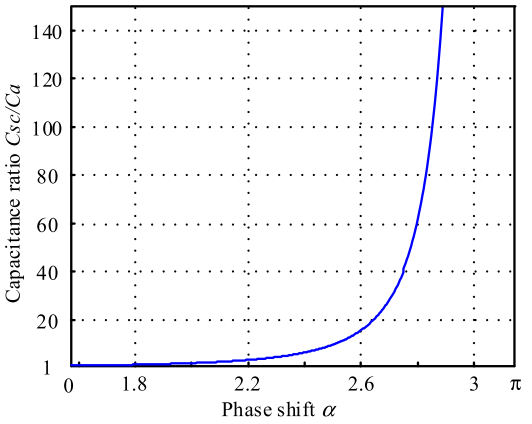

FIGURE 2. Capacitance ratio C_{sc} /C_a versus phase shift α.

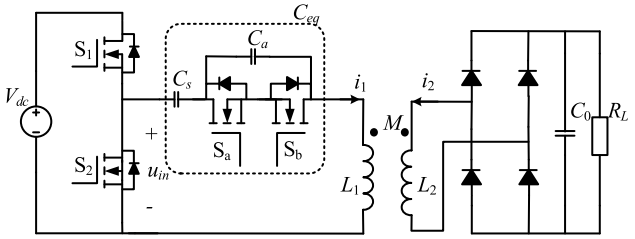

FIGURE 3. Structure of the proposed WPT system.

B. CIRCUIT CONFIGURATION

Figure 3 shows the circuit configuration of the proposed WPT system. As shown in Figure 3, the circuit of the WPT system consists of a half-bridge inverter; a SCC; a series capacitor; a pair of coupled coils; a diode full-bridge rectifier; filter and the load. The SCC is connected in series with the capacitor C_s to regulate the equivalent capacitance C_{eq}. The equivalent capacitance of the SCC is given in (5). The total equivalent capacitance C_{eq} is

$$C_{eq} = \frac{C_{sc}C_s}{C_{sc}+C_s} = \frac{\pi C_a C_s}{\pi C_a + C_s(2\pi - 2\alpha + \sin(2\alpha))} \tag{6}$$

The power is transferred by the coupled coils and the mutual inductance M of the coupled coils is

$$M = \kappa\sqrt{L_1 L_2} \tag{7}$$

where L_1 and L_2 are the inductance of the transmitting coil and receiving coil, respectively. κ is the coupling coefficient of the coils.

Then, if power switches S_1 and S_2 are appropriately controlled, the DC voltage V_{dc} will be chopped as a square waveform in high frequency. This square voltage u_{in} then be fed into the resonant tank consisting of the adjustable capacitor C_{eq} and the coupled coils and then sinusoidal voltage component is extracted into the coupled coils. Power switches S_1 and S_2 are complementarily triggered with leading edge delays under asymmetrical PWM (APWM) control [19]. The voltage u_{in} at the input terminal of the SCC can be represented

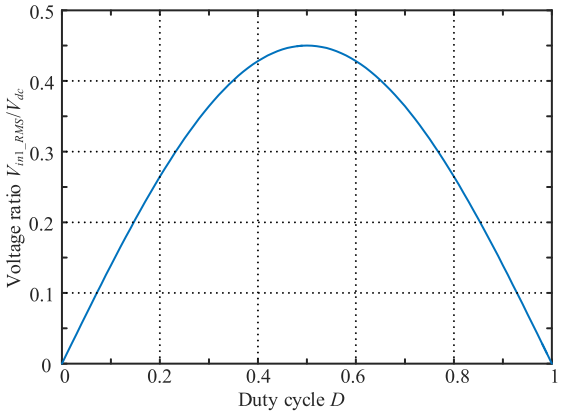

FIGURE 4. Voltage ratio as a function of duty cycle D.

by the following Fourier series,

$$u_{in} = V_{dc}D + \sum_{n=1}^{\infty} \frac{\sqrt{2}V_{dc}\sqrt{1-\cos(2n\pi D)}}{n\pi} \sin(n\omega_0 t + \theta_n) \tag{8}$$

where D and ω_0 are the duty cycle for switch S_1 and switching angular frequency, respectively, and

$$\theta_n = \arctan\left(\frac{\sin(2n\pi D)}{1-\cos(2n\pi D)}\right) \tag{9}$$

Only the AC fundamental component of the voltage u_{in} does contribution to the power transfer control due to the DC block capacitor and the resonant tank. The RMS value and the phase angle of fundamental component of u_{in} are given as

$$V_{in1\_RMS} = \frac{V_{dc}}{\pi}\sqrt{1-\cos(2\pi D)} \tag{10}$$

$$\theta_1 = \arctan\left(\frac{\sin(2\pi D)}{1-\cos(2\pi D)}\right) \tag{11}$$

Figure 4 shows the voltage ratio as a function of duty cycle D. which is obtained from (10). It can be observed that the voltage ratio increased with increment of D from 0 to 0.5, and decreased with reduction of D from 0.5 to 1. The maximum voltage ratio appears at $\alpha = \pi$.

III. OPERATION MODES OF WPT SYSTEM

A. EQUIVALENT CIRCUIT

To analysis the characteristics of the WPT system, the fundamental harmonic analysis model is given in Figure 5(a). The equivalent series resistances (ESRs) R_1 and R_2 are used to represent the power losses, such as conduction loss of the coils and switches, switching loss and radiation loss. Normally, the variation of the ESRs according to the operating conditions is very small. To simplify the analysis, the ESR*s* are considered as constant. R_{eq} is the equivalent AC load resister that stands for the input resistance of the rectifier. The relationship between R_{eq} and the load R_L is

$$R_{eq} = \frac{8}{\pi^2}R_L \tag{12}$$

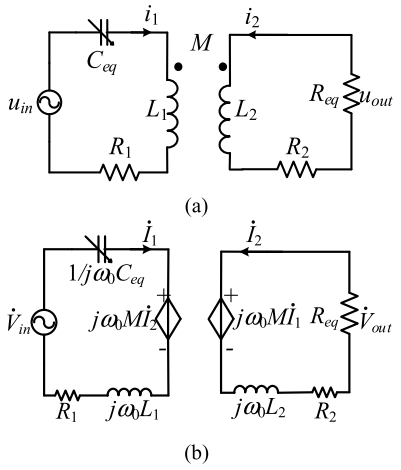

FIGURE 5. Equivalent circuit. (a) Fundamental harmonic analysis model; (b) equivalent decoupling circuit.

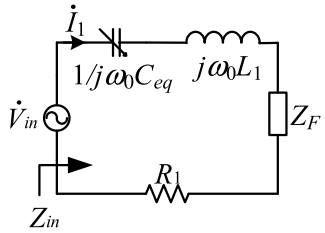

FIGURE 6. Resonance analysis of the proposed circuit.

To simplify the analysis, the coupled coils are decoupled by adding two current-controlled voltage sources, as shown in Figure 5(b). According to the Kirchhoff's voltage law, the proposed WPT system can be described by the following equations

$$\begin{cases} (R_1 + j(\omega_0 L_1 - 1/\omega_0 C_{eq}))\dot{I}_1 + j\omega_0 M\dot{I}_2 = \dot{V}_{in} \\ j\omega_0 M\dot{I}_1 + (j\omega_0 L_2 + R_2 + R_{eq})\dot{I}_2 = 0 \\ -\dot{I}_2 R_{eq} = \dot{V}_{out} \end{cases} \quad (13)$$

where $\dot{V}_{in}$ and $\dot{V}_{out}$ are the phases of fundamental harmonics of the AC input voltage and the AC output voltage, respectively; $\dot{I}_1$ and $\dot{I}_2$ are the phases of the inductors' current, and j is the imaginary unit.

B. RESONANCE CONDITION OF THE INVERTER

By reflecting the secondary side to the primary side, the circuit can be simplified as Figure 6. Then the reflected impedance can be expressed as

$$Z_F = \frac{(\omega_0 M)^2}{R_2 + R_{eq} + j\omega_0 L_2} \quad (14)$$

Equation (14) is shown that the reflected impedance of the secondary side is capacitive. If the input impedance of the WPT system is capacitive also, then the system will fail to achieve the ZVS operation. Therefore, the adjustable capacitor is adopted to compensate the input impedance with an inductive load characteristic. In this case, the inverter can achieve ZVS operation. The input impedance of the WPT system can be derived as

$$Z_{in} = R_1 + j(\omega_0 L_1 - \frac{1}{\omega_0 C_{eq}}) + Z_F = |Z_{in}| \angle\varphi \quad (15)$$

where φ is the impedance angle that can be found from the phase difference between the input voltage $u_{in\ 1}$ and the current i_1. In order to perform the ZVS operation of the inverter switches, the current should go through the diode of the switches before triggering, meaning that Z_{in} needs to be inductive as mentioned above to form a lagging current.

In this way, the input impedance angle φ should be selected to be larger than the phase angle θ_1 in (11)

$$\varphi \geq \arctan(\frac{\sin(2\pi D)}{1 - \cos(2\pi D)}) \quad (16)$$

The ZVS operation can be built up by meeting the inequality constraint of (16). It should be noted that (16) is only a necessary but not sufficient condition for ZVS condition because parasitic capacitances, such as output capacitance of switch devices and stray capacitance require enough energy from inductance for charging and discharging during dead time. In other word, the phase angle $\varphi - \theta_1$ should be larger than the dead time setting of switches.

Figure 7 shows the operation modes of inverter and typical waveforms with following assumed.

1) The output capacitances of MOSFETs has the same values.

2) The resonant current is approximated to be sinusoidal. According to the current flow, we divide the operation of the inverter into six modes

Mode 1 [t_0, t_1]: The resonant current flow is highlighted, and the rest of circuit is faded. At time t_0, S_2 is turned off. The triggering signal of S_1 is delayed to prevent S_1 and S_2 from being shorted. At this situation, the energy is delivered from load to source.

Mode 2 [t_1, t_2]: As shown in Mode 2 of Figure7(b), at time t_1, the triggering signal of S_1 is raised to active S_1, the resonant current is negative as same to Mode 1 and flows though diode D_1, then, S_1 turns on at zero voltage.

Mode 3 [t_2, t_3]: after time t_2, the resonant current becomes positive, and through the S_1 and resonant circuit from the other direction. The energy is transferred from DC to the resonant circuit until the triggering signal of S_1 is removed.

Mode 4 [t_3, t_4]: At time t_3, S_1 is turned off. The resonant current is still positive and flowing through the diode D_2 of S_2 as shown in Mode 4 of Figure 7(b). The triggering signal of S_2 is delayed to trigger, entering the dead time interval to prevent S_1 and S_2 from being shorted.

Mode 5 [t_4, t_5]: at time t_4, the triggering signal of S_2 is raised to active S_{12}, the resonant current is negative as same to Interval 4 and flows though diode D_2, then, S_2 turns on at zero voltage.

Mode 6 [t_5, t_6]: after time t_5, the resonant current becomes negative, and through the S_2 and resonant circuit from the other direction. At time t_6, the switching period is completed, and the same operation continues.

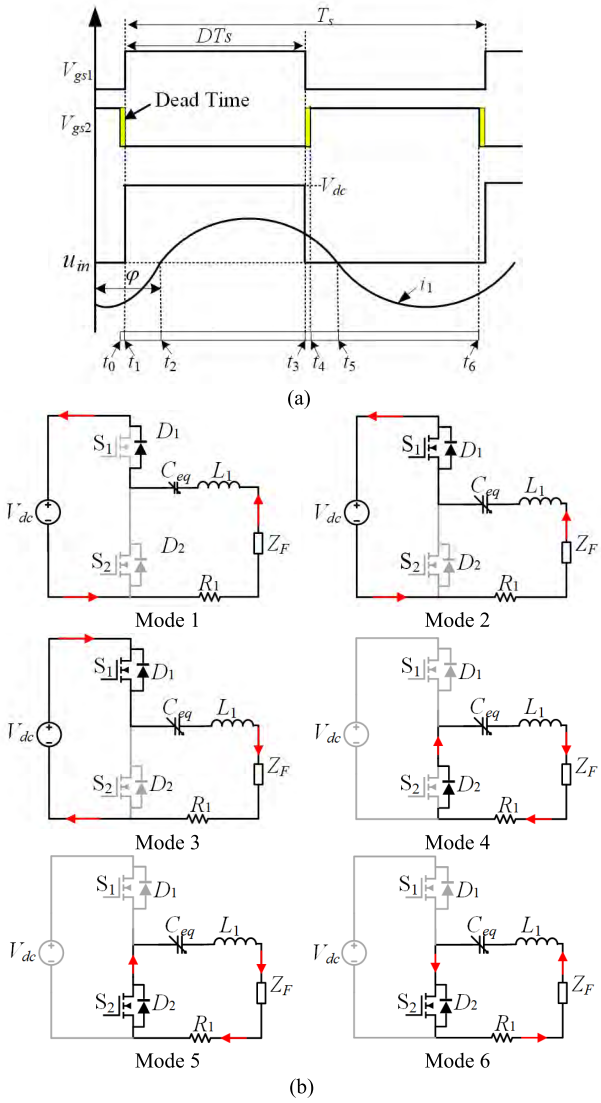

FIGURE 7. Operation modes of inverter. (a) Typical waveforms, (b) current flow of resonant circuit at each interval.

IV. CONTROL STRATEGY

A. REGULATION OF EQUIVALENT CAPACITANCE

According to the impedance matching rule, the equivalent capacitance C_{eq} with maximum voltage gain could be obtain by removing imaginary part of the impedance Z_{in} shown in (15). It is

$$C_{eq} = \frac{(R_2 + R_{eq})^2 + (\omega_0 L_2)^2}{((R_2 + R_{eq})^2 + (\omega_0 L_2)^2)\omega_0^2 L_1 + \omega_0^4 M^2 L_2} \quad (17)$$

The equivalent capacitance C_{eq} should be regulated by (6) to meet the requirement of (17), and then the system will be operated at the supposed resonant frequency. The voltage gain is defined based on the AC input voltage $\dot{V}_{in}$ and the AC output voltage $\dot{V}_{out}$, and it has

$$G_v = \frac{j\omega_0 M R_{eq}}{(R_1 + j(\omega_0 L_1 - \frac{1}{\omega_0 C_{eq}}))(R_2 + R_{eq} + j\omega_0 L_2) + (\omega_0 M)^2} \quad (18)$$

TABLE 1. Parameters of inverter system.

Symbol	Quantity	Value
L_1	Inductance of primary coil	100 μH
L_2	Inductance of secondary coil	100 μH
R_1, R_2	ESR	0.5 Ω
M	Mutual inductance	12 μH
R_{eq}	Equivalent AC load	6 Ω

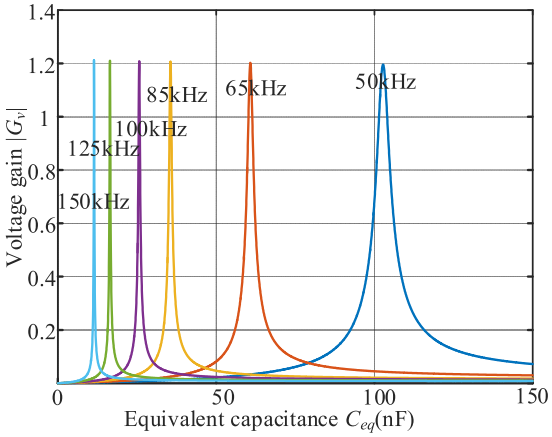

FIGURE 8. Voltage gain versus equivalent capacitance C_{eq}.

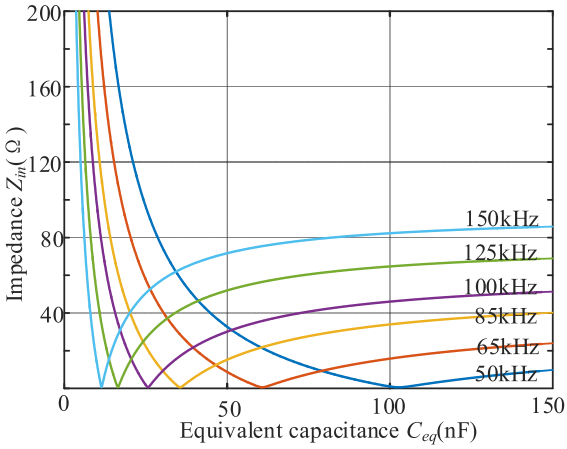

FIGURE 9. Input impedance versus equivalent capacitance C_{eq}.

Table 1 shows the parameters of the inverter system. With the parameters listed in Table 1, the voltage gain as function of equivalent capacitance C_{eq} is given in Figure 8. When $f_0 = 100$ kHz, the value of C_{eq} is calculated as 25.7nF by (17). Figure 8 is shown that the maximum gain can be achieved at the point of 102.7nF, 60.8 nF, 35.3 nF, 25.7 nF, 16.5 nF and 11.4 nF for equivalent capacitance C_{eq}, where f_0 is 50 kHz, 65kHz, 85kHz, 100kHz, 125kHz and 150kHz, respectively. However, the input impedance is very low at such point with maximum gain, as shown in Figure 9. Then large input current would be caused by low input impedance and may threat the safety operations of the inverter, resonant capacitor,

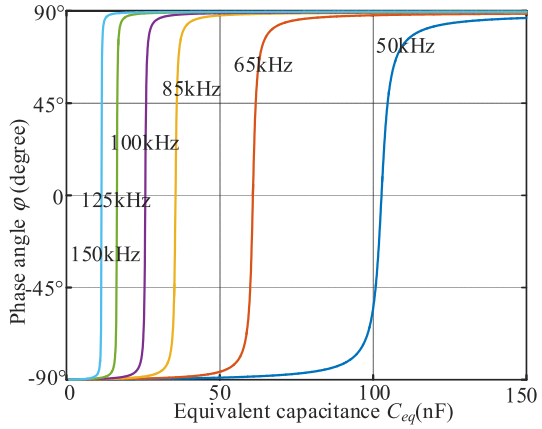

FIGURE 10. Phase angle curves of input impedance under different operating frequency.

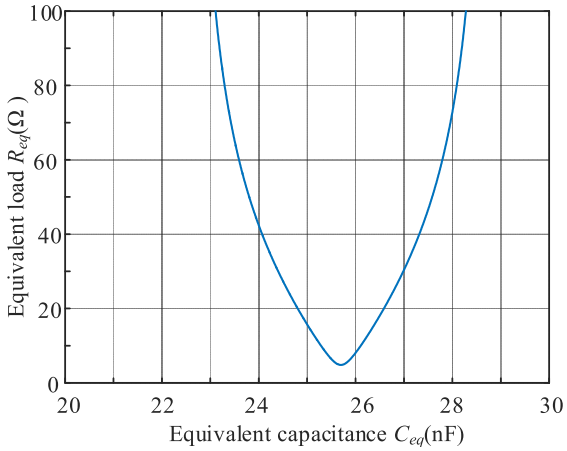

FIGURE 11. Equivalent capacitance C_{eq} versus various equivalent load R_{eq}.

and primary coil. Therefore, the equivalent capacitance C_{eq} needs to be regulated to offset the maximum voltage gain.

Figure 10 shows the phase angle curve of input impedance under the different operating frequency. As the frequency f_0 is set at 50 kHz and the value of C_{eq} is less than 102.7 nF, the inverter system will not realize ZVS operation because of the capacitive load characteristics. It should be noted that once certain operating frequency is determined, the regulated equivalent capacitance should be larger than the capacitance value with the maximum voltage gain at same frequency, which ensures the load with inductive characteristics.

Figure 11 shows the equivalent capacitance C_{eq} versus various equivalent loads R_{eq} based on the given parameters of $f_0 = 100$ kHz and $|G_v| = 1.0$. Obviously, the equivalent capacitance C_{eq} is regulated via the phase shift angle α to track the operating frequency and voltage gain. Base on the given parameters of f_0 and $|G_v|$, there are two roots for C_{eq} with a given equivalent load R_{eq}, as shown in Figure 11. In other words, there are two capacitance points for C_{eq} to stabilize the load: one load with capacitive characteristics and another load with inductive characteristics. The larger root of C_{eq} would be favorable because the equivalent load

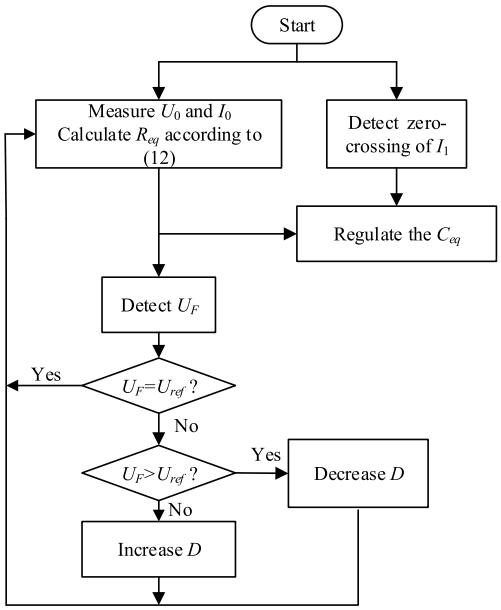

FIGURE 12. Flowchart of the control strategy for the half-bridge inverter.

is inductive in this case, which may realize ZVS operation for the high-frequency inverter.

B. CONTROL METHOD

A control strategy is designed for the effective operation of the proposed WPT system. Figure 12 gives the flowchart of the control strategy. As shown in Figure 12, the operating frequency and voltage gain of the system should be first determined. The control strategy starts by measuring the output voltage and current, and then, calculating the equivalent load R_{eq}. Based on the equivalent load, the equivalent capacitance C_{eq} is regulated. When the feedback signal U_F is bigger than the reference signal U_{ref}, the duty cycle D is reduced. Yet, when the feedback signal U_F is less than the reference signal U_{ref}, the duty cycle D is increased to keep the output voltage stable.

In addition, by considering the system stability, the feedback control is implemented, as shown in Figure13. The feedback signals of voltage and current obtained by the RF modules are transferred wirelessly to provide for SCC PWMs and APWM generation. The detection of the equivalent load is processed for a given operating frequency and voltage gain. The adjusted duty cycle values are then used to control the SCC PWMs. The SCC PWMs are synchronized with the zero crossing points of the primary side current of the corresponding phase.

V. EXPERIMENTAL VERIFICATIONS

A. EXPERIMENTAL PLATFORM SETUP

In order to investigate the feasibility of the proposed system, a hardware prototype has been implemented and tested in the laboratory. The experimental setup of the proposed system is shown in Figure 13, and the parameters of the experimental platform are listed in Table 2.

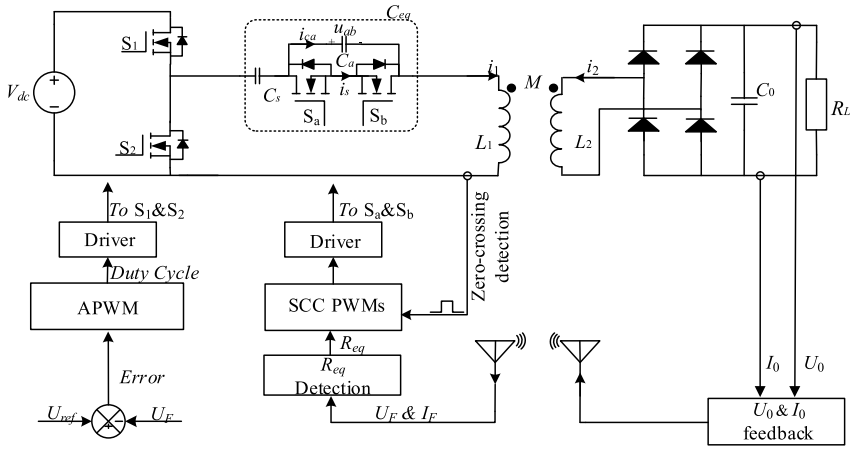

FIGURE 13. System block diagram with the proposed control strategy.

TABLE 2. Parameters of experimental platform.

Symbol	Quantity	Value
L_1	Primary coil inductance	99.89 µH
L_2	Secondary coil inductance	100.02 µH
N_1	Number of primary coils	20 turns
N_2	Number of secondary coils	20 turns
R_1 , R_2	ESR	0.4 Ω
M	Mutual inductance	12.04 µH
C_s	Series capacitor	66 nF
C_a	SCC capacitor	15 nF
C_0	Output capacitor	470 µF

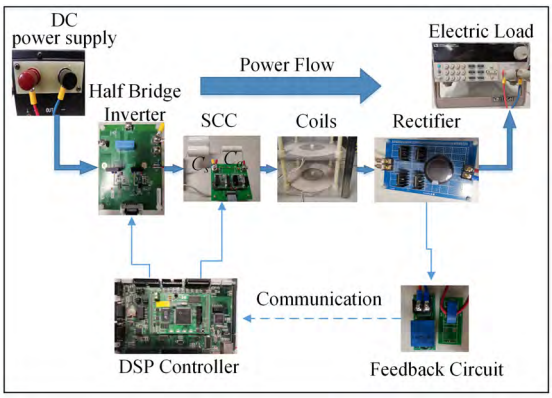

FIGURE 14. Experimental platform of the proposed system.

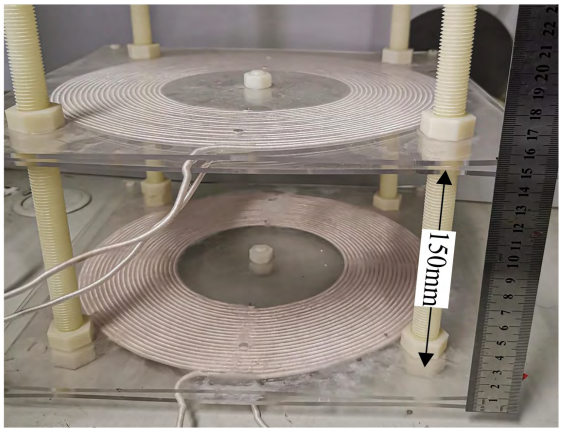

FIGURE 15. Structure of coupled coils.

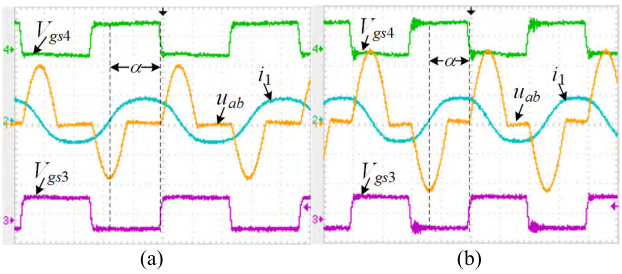

FIGURE 16. Measured waveforms of SCC modulation under different operating frequency. (u_{ab}:200 V/div; V_{gs3}:20 V/div; V_{gs3}:20 V/div; i_1:10 A/div; T:2.5 μs).

As shown in Figure 14, the power starting from a DC power supply flows through the half bridge inverter, the SCC, the coupled coils and the full bridge rectifier. Finally, it provides to the electrical load which serves as the adjustable load resister. The inverter and the SCC are controlled by the PWM interfaces from digital signal processor (DSP) controller based on the feedback signals of the load. The feedback signals are transferred by the communication link. As shown in Figure 15. The coupled coils are made of Litz wire. The structure of coils directly faces each other and turn numbers of primary coil and the secondary coil are all 20. The original distance between them is 150 mm. However, when the coils are misaligned, the mutual inductance M may be varied, and the voltage gain is changed. Then the SCC would be regulated to achieve a stable voltage gain.

B. EXPERIMENTAL RESULTS

Figure 16 shows the measured waveforms of the SCC with modulation under different operating frequency, where u_{ab} is the voltage across the parallel capacitor C_a, i_1 is the current

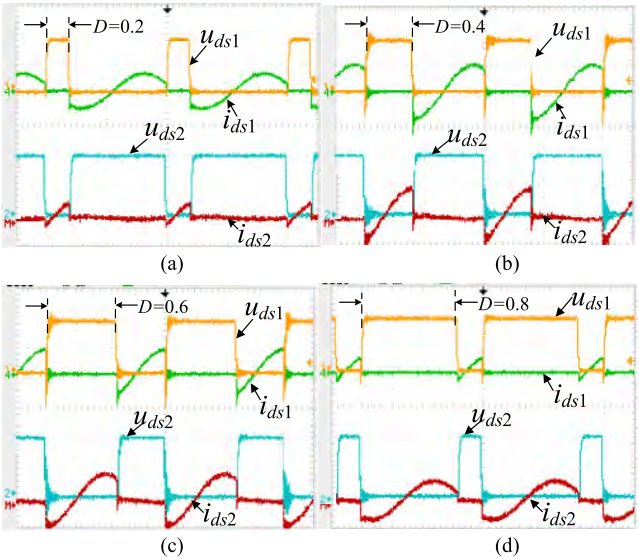

FIGURE 17. ZVS operation with (a) D = 0.2; (b) D = 0.4; (c) D = 0.6; (d) D = 0.8. (u_{ds1}:10 V/div; u_{ds2}:10 V/div; i_{ds1}:10 A/div; i_{ds2}:10 A/div; T:2.5 μs).

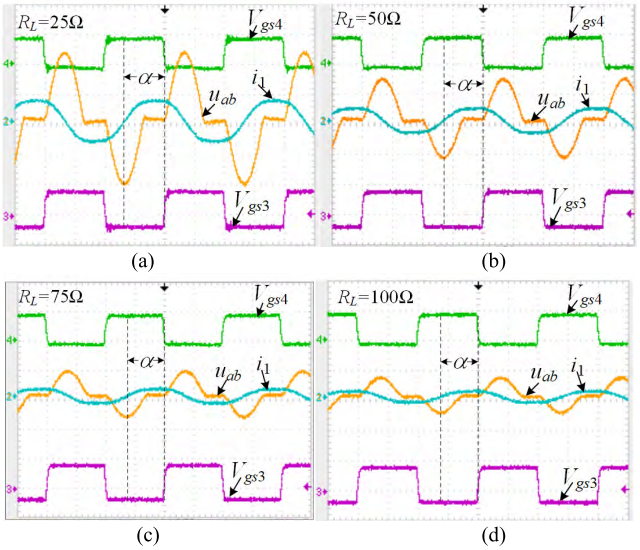

FIGURE 18. Measured waveforms of Ceq with various loads R_L. (u_{ab}:200 V/div; V_{gs3}:20 V/div; V_{gs3}:20 V/div; i_1:10 A/div; T:2.5 μs).

through the SCC, V_{gs4} is the gate signal of S_4 and V_{gs3} is the gate signal of S_3. Figure 16 (a) shows the scenario with operating frequency 85 kHz and the control angle 137.3°. Figure 16 (b) shows the scenario with operating frequency 100 kHz and the control angle 144.0°. In addition, because u_{ab} is always zero at turn-on and turn-off points, implying that switch S_a and S_b are switched both ON and OFF at ZVS conditions.

Figure 17 shows the measured waveforms of the half inverter switches under different duty cycle, where u_{ds1} and u_{ds2} are the drain-source voltage of the switch S_1 and S_2, respectively, i_{ds1} and i_{ds2} are the current through the switch S_1 and S_2, respectively. The waveforms of drain-source voltage and current under the duty cycles with 0.2, 0.4, 0.6 and 0.8 are individually measured. It is clearly shown that the current i_{ds1} and i_{ds2} change from negative to positive when each switch S_1 or S_2 is turned on. In other words, the current flows through the parallel-diode of each switch before it is activated, thereby confirming that the inverter effectively performs the ZVS operation.

To maintain a stable output voltage, the equivalent capacitance C_{eq} is regulated to keep a constant voltage gain as the load changes. Figure 18 shows C_{eq} with various loads R_L based on the selection of $f_0 = 100$ kHz. Figure 18(a) shows the SCC operation when the load was 25 Ω. Here, the control angle is measured as 122.6°, the C_{eq} is calculated as 26.05nF. Hence, the inverter maintains an inductive load state and an adequate voltage gain with $|G_v| = 2.0$. Figure 18(b) shows the SCC operation when the load was 50 Ω. Here, the control angle is measured as 124.3°, the C_{eq} is calculated as 27.30nF. Figure 18(c) shows the SCC operation when the load was 75 Ω. Here, the control angle is measured as 125.4°, the C_{eq} is calculated as 28.15nF. Figure 18(d) shows the SCC operation when the load was 100 Ω. Here, the control angle is measured as 125.8°, the C_{eq} is calculated as 28.42 nF. These results prove that the proposed WPT system is highly flexible, because it provides constant output voltage against load variations. That is very practical for industry applications, especially for battery charging.

TABLE 3. Comparisons.

Reference	Resonant tuning element	Purpose
This paper	PWM capacitor	Impedance compensation for WPT
[4] @2018	PWM capacitor	Efficiency improvement for WPT
[21] @2018	Capacitor arrays	Component optimization for WPT
[22] @2018	Capacitor arrays	Capacity expansion for plasma applications

C. COMPARISON

The comparisons of the proposed method and previous techniques are shown in Table 3, where different control methods and purposes are used for the resonant tuning element with variable capacitance. In [21] and [22], the capacitor arrays are applied to select the suitable capacitance, which are bulky and cannot generate a continuous capacitance regulation. In [4], a PWM-controlled capacitor was proposed to realize self-tuning of the LCC converter. Since the capacitance value is regulated by single switch with varied PWM on/off duty ratio, the voltage stress will be high, and the range of variable capacitance is very small. In this paper, the load impedance is compensated by regulating the SCC. At the same time, the modulation of the SCC guarantees an inductive input impedance of WPT system, achieving soft switching and reducing the high switching losses of the high-frequency inverter.

VI. CONCLUSION

In this paper, a SCC is adopted in the primary side of the WPT system. The SCC can regulate equivalent capacitance easily which makes it flexible to control the resonance point of the high-frequency inverter. So, it can not only compensate the leakage of the coupled coils and large manufacturing tolerance, but also ensure inductive impedance for the WPT system, which achieves soft switching operation and reduces switching losses greatly for high-frequency inverter. The capacitance of the SCC can be regulated according to the operating frequency and the load variations. A prototype is built to verify the feasibility of the proposed WPT system, and through the experiment results, it is validated that the inverter effectively performs the ZVS operation. Meanwhile, various load conditions have been applied to verify the performance of the proposed system.

REFERENCES

[1] A. Kurs, A. Karalis, R. Moffatt, J. D. Joannopoulos, P. Fisher, and M. Soljačić, "Wireless power transfer via strongly coupled magnetic resonances," *Science*, vol. 317, no. 5834, pp. 83–86, 2007.

[2] S. Y. R. Hui, W. Zhong, and C. K. Lee, "A critical review of recent progress in mid-range wireless power transfer," *IEEE Trans. Power Electron.*, vol. 29, no. 9, pp. 4500–4511, Sep. 2014.

[3] S. A. Mirbozorgi, H. Bahrami, M. Sawan, and B. Gosselin, "A smart multicoil inductively coupled array for wireless power transmission," *IEEE Trans. Ind. Electron.*, vol. 61, no. 11, pp. 6061–6070, Nov. 2014.

[4] D. Kim and D. Ahn, "Self-tuning LCC inverter using PWM-controlled switched capacitor for inductive wireless power transfer," *IEEE Trans. Ind. Electron.*, vol. 66, no. 5, pp. 3983–3992, May 2018.

[5] D. Ahn and S. Hong, "Wireless power transmission with self-regulated output voltage for biomedical implant," *IEEE Trans. Ind. Electron.*, vol. 61, no. 5, pp. 2225–2235, May 2014.

[6] J. Sallan, J. L. Villa, A. Llombart, and J. F. Sanz, "Optimal design of ICPT systems applied to electric vehicle battery charge," *IEEE Trans. Ind. Electron.*, vol. 56, no. 6, pp. 2140–2149, Jun. 2009.

[7] C. Liu, K. T. Chau, D. Wu, and S. Gao, "Opportunities and challenges of vehicle-to-home, vehicle-to-vehicle, and vehicle-to-grid technologies," *Proc. IEEE*, vol. 101, no. 11, pp. 2409–2427, Nov. 2013.

[8] C. Y. Lee, J. H. Lee, J. M. Jo, C. B. Park, W. H. Ryu, Y. D. Chung, Y. J. Hwang, T. K. Ko, S.-Y. Oh, and J. Lee, "Conceptual design of superconducting linear synchronous motor for 600-km/h wheel-type railway," *IEEE Trans. Appl. Supercond.*, vol. 24, no. 3, p. 3600304, Jun. 2014.

[9] M. K. Uddin, G. Ramasamy, S. Mekhilef, K. Ramar, and Y.-C. Lau, "A review on high frequency resonant inverter technologies for wireless power transfer using magnetic resonance coupling," in *Proc. IEEE CENCON*, Malaysia, Oct. 2014, pp. 412–417.

[10] A. P. Sample, D. T. Meyer, and J. R. Smith, "Analysis, experimental results, and range adaptation of magnetically coupled resonators for wireless power transfer," *IEEE Trans. Ind. Electron.*, vol. 58, no. 2, pp. 544–554, Feb. 2011.

[11] N. Y. Kim, K. Y. Kim, J. Choi, and C.-W. Kim, "Adaptive frequency with power-level tracking system for efficient magnetic resonance wireless power transfer," *Electron. Lett.*, vol. 48, no. 8, pp. 452–454, Apr. 2012.

[12] H. Li, J. Li, K. Wang, W. Chen, and X. Yang, "A maximum efficiency point tracking control scheme for wireless power transfer systems using magnetic resonant coupling," *IEEE Trans. Power Electron.*, vol. 30, no. 7, pp. 3998–4008, Jul. 2015.

[13] M. Fu, C. Ma, and X. Zhu, "A cascaded boost-buck converter for high efficiency wireless power transfer systems," *IEEE Trans. Ind. Informat.*, vol. 10, no. 3, pp. 1972–1980, Aug. 2014.

[14] T. C. Beh, M. Kato, T. Imura, S. Oh, and Y. Hori, "Automated impedance matching system for robust wireless power transfer via magnetic resonance coupling," *IEEE Trans. Ind. Electron.*, vol. 60, no. 9, pp. 3689–3698, Sep. 2013.

[15] S. Li, W. Li, J. Deng, and C. C. Mi, "A double-sided LCC compensation network and its tuning method for wireless power transfer," *IEEE Trans. Veh. Technol.*, vol. 64, no. 6, pp. 1–12, Jun. 2015.

[16] J. Shin, S. Shin, Y. Kim, S. Ahn, S. Lee, G. Jung, S.-J. Jeon, and D.-H. Cho, "Design and implementation of shaped magnetic-resonance-based wireless power transfer system for roadway-powered moving electric vehicles," *IEEE Trans. Ind. Electron.*, vol. 61, no. 3, pp. 1179–1192, Mar. 2014.

[17] X. Liu, T. Wang, X. Yang, N. Jin, and H. Tang, "Analysis and Design of a Wireless Power Transfer System with Dual Active Bridges," *Energies*, vol. 10, no. 10, p. 1588, Oct. 2017.

[18] Z. Hu, Y. Qiu, L. Wang, and Y.-F. Liu, "An interleaved LLC resonant converter operating at constant switching frequency," *IEEE Trans. Power Electron.*, vol. 29, no. 6, pp. 2931–2943, Jun. 2014.

[19] F. S. Pai, C. L. Ou, and S. J. Huang, "Plasma-driven system circuit design with asymmetrical pulsewidth modulation scheme," *IEEE Trans. Ind. Electron.*, vol. 58, no. 9, pp. 4167–4174, Sep. 2011.

[20] J.-H. Jung, H.-S. Kim, M.-H. Ryu, and J.-W. Baek, "Design methodology of bidirectional CLLC resonant converter for high-frequency isolation of DC distribution systems," *IEEE Trans. Power Electron.*, vol. 28, no. 4, pp. 1741–1755, Apr. 2013.

[21] J. Osawa, T. Isobe, and H. Tadano, "Efficiency improvement of high frequency inverter for wireless power transfer system using a series reactive power compensator," in *Proc. IEEE 12th Int. Conf. Power Electron. Drive Syst.*, Dec. 2017, pp. 992–998.

[22] T. Lee, S. Huang, K. Huang, and P. Chiang, "Modular design and analysis of plasma-driven system with integrated resonant circuit and capacity expansion mechanism," *IEEE Trans. Power Electron.*, vol. 65, no. 2, pp. 1226–1234, Feb. 2018.

JIN ZHAO (S'16) received the M.Sc. degree in electrical engineering from the Jiangsu University of Science and Technology, Zhenjiang, China, in 2014. He is currently pursuing the Ph.D. degree with the Department of Electrical Engineering, Southeast University, Nanjing, China.

Since December 2018, he has been with The University of British Columbia, Vancouver, Canada, where he is currently a joint Ph.D. student with the Electrical Power and Energy Systems (EPES) Research Group, Faculty of Applied Science. His research interests include resonant power converters, wireless power transfer, and electric machines and drives.

JIANZHONG ZHANG (M'08–SM'16) received the M.Sc. and Ph.D. degrees in electrical engineering from the Department of Electrical Engineering, Southeast University, Nanjing, China, in 2005 and 2008, respectively.

From 2006 to 2007, he was a Visiting Scholar with the Department of Energy Technology, Aalborg University, Aalborg, Denmark. Since 2008, he has been with Southeast University, where he is currently a Research Professor with the School of Electrical Engineering. He was a Visiting Professor with the Worcester Polytechnic Institute, Worcester, MA, USA, in July 2012. His research interests include electric machines, power electronics, and wind power generation.

Dr. Zhang is a recipient of the Institution Premium Award of the Institutions of Engineering and Technology, U.K.

YAODONG ZHU received the M.Sc. and Ph.D. degrees in test measurement technology and instrument from the Department of Automation, Nanjing University of Aeronautics and Astronautics, Nanjing, China, in 2000 and 2003, respectively.

Since 2005, he has been with Jiaxing University, where he is currently an Associate Professor with the School of Mechanical and Electrical Engineering. His research interests include smart robot, embedded computing, and computer vision.